Forward Looking Ground Penetrating Radar via a linear inverse scattering approach

Ilaria Catapano[1], *Member, IEEE, Antonio Affinito*[1], *Alessio Del Moro*[2], *Giovanni Alli*[2],

Francesco Soldovieri[1] *Fellow, IEEE*

[1]Institute for Electromagnetic Sensing of the Environment – IREA, National Research Council of Italy – CNR, Via Diocleziano 328, I-80124 Napoli, Italy.

[2]IDS-Ingegneria dei Sistemi S.p.a., Via Enrica Calabresi, 24, I-56121, Pisa, Italy.

Abstract – An inverse scattering approach has been designed to process data gathered by means of forward looking ground penetrating radar systems. Such an inverse approach exploits a linear model of the scattering phenomenon and is able to account for the half-space 2D geometry. In this frame, a theoretical study on the achievable reconstruction capabilities is provided with the aim to estimate the range and cross-range resolution limits and gain indications about the issue of how to design the measurement configuration. Finally, numerical and experimental examples are provided to assess the effectiveness of the approach.

Keywords: Forward Looking GPR; inverse scattering; resolution limits; experimental data

I. Introduction

Forward looking ground penetrating radar (FLGPR) systems are gaining attention as subsurface imaging tools, owing to their capability of assuring a standoff distance between the operator and the targets. This capability is particularly important when potentially dangerous objects have to be detected and localized, as for landmine and improvised explosive device (IED) detection [1-4].

With respect to the most common down looking systems, the design of FLGPR is complicated by the constraints about the measurement configuration, which entails severe limitations for the angle of view and the energy of received target echo. Therefore, significant efforts are continuously addressed towards the set-up of advanced hardware solutions and imaging approaches able to overcome the above said difficulties [4-13].

This paper proposes an imaging approach belonging to the family of the linear inverse scattering procedures in a 2D geometry. Similar imaging approaches have been already successfully adopted in the frame of GPR data collected by means of down-looking [14-17] and airborne [18] systems.

With respect to the approach presented in [11], here the hypothesis of homogeneous free-space scenario is removed and the presence of the air-soil interface is taken into account in the scattering model by assuming half-space geometry. This is performed by exploiting suitable expressions of the incident field and the Green's function, which are the key ingredients of the linear integral equation to be inverted, i.e. the equation relating the scattered field to the contrast function. This permits to accurately model the FLGPR configuration, where the antennas are located at a non-negligible distance (in terms of probing wavelength) from the ground surface and the spatial domain under test. Therefore, the main contributions of this paper can be summarized as follows:

1) development of a linear inverse scattering approach specifically designed to process FLGPR data;

2) analysis of the reconstruction capabilities achievable by means of the linear inverse model of the scattering under FLGPR configuration;

3) assessment of the effectiveness of the linear inverse scattering approach with numerical and experimental data.

The analysis of the reconstruction capabilities is performed with the aim to estimate the theoretical bounds for the range and cross-range resolution limits as well as to provide guidelines to select the extent of the measurement lines according to the spatial size and position of the investigated domain. These guidelines drive the design of optimized and non-redundant radar measurement arrangements able to produce accurate subsurface imaging results.

The theoretical expectations achieved by means of a ray-based model are after confirmed by a numerical analysis, which exploits the assessed tools of the spectral content and the regularized point spread function [19, 20].

Finally, an assessment of the achievable imaging capabilities is carried out thanks to a numerical analysis and the validation with experimental data, which represents a preliminary test of the actual performance in realistic conditions. In this frame, we also discuss the detrimental effects produced on the imaging results by misestimating the soil's permittivity as well as by wrongly adopting the free-space model.

The paper is organized as follows. The imaging approach is described in the next section, while the analysis of the achievable reconstruction capabilities is presented in section III. Numerical examples and the experimental assessment are provided in section IV. Conclusions follow.

II. The imaging approach

Let us consider the reference geometry in Fig.1 regarding 2D half-space geometry, where the upper half-space is air whereas the lower one is modelled as a non-magnetic homogeneous medium having relative dielectric permittivity ε_{br}, electric conductivity σ_b and magnetic permeability μ_0. The investigated spatial domain is denoted as *D* and it is probed by a filamentary electric current linearly polarized along the *y*-axis with unitary amplitude. The time dependence is assumed equal to exp(jωt) and omitted. A multi-bistatic configuration is deployed, where the transmitting and receiving antennas are at different heights h_t and h_r from the air-soil

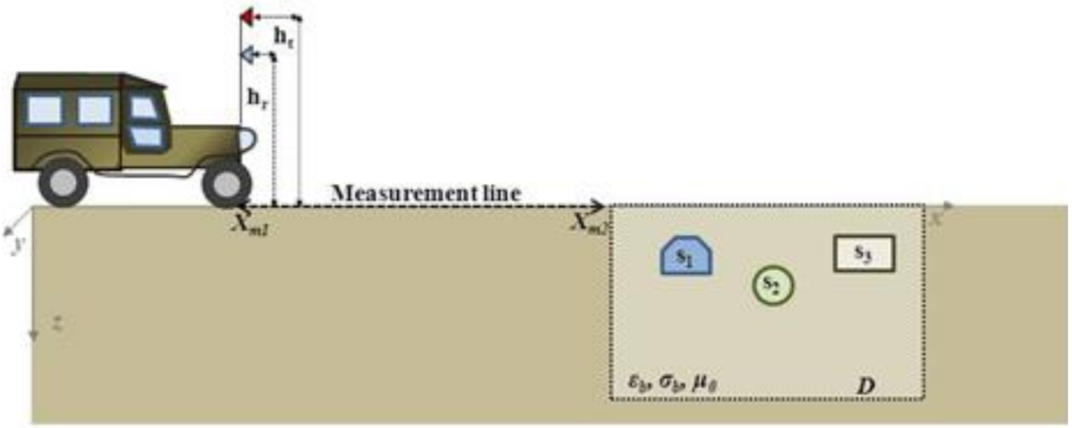

Fig.1 Reference geometry

interface, respectively, and are moved along a straight scanning line, whose extremes are [X_{m1}, X_{m2}]. A multi-frequency configuration is considered with a frequency range [$f_{\min}$, $f_{\max}$].

According to 2D geometry, the scatterers are schematized as cylinders of arbitrary cross section in the (x-z) plane, whose dielectric (possibly complex) permittivity $\varepsilon_t(x,z)$, is related to that of the host medium, ε_b, by means of the contrast function:

$$\chi(x,z)=\frac{\varepsilon_t(x,z)}{\varepsilon_b}-1 \tag{1}$$

Here, a Born inverse model is considered; the effectiveness of the Born inverse model to provide information about location and geometry of the targets has been proved in many cases even for strongly scattering targets (see [16, 21, 22]).

On the other hand, the adoption of the Born model makes it impossible to achieve a quantitative reconstruction of the targets (in terms of electromagnetic properties) and to account for the mutual interactions between the targets (similarly to any linear inverse scattering approach) [23].

Under the Born model, at each angular frequency $\omega=2\pi f$ and for each position of the antenna system, the relationship between the contrast function and the scattered field data is given by [19]:

$$E_s\left(x_T, h_t, x_R, h_r, \omega\right) = k_b^2 \int_D G\left(x_r, h_r, \omega, \underline{r}\right) E_{inc}\left(x_t, h_t, \omega, \underline{r}\right) \chi\left(\underline{r}\right) d\underline{r} \qquad (2)$$

In eq.(2), k_b is the wave-number in the probed soil at the angular frequency ω, E_{inc} is the incident field radiated by the transmitting antenna located at (x_t, h_t) in the generic point $\underline{r}$ = (x, z) belonging to the investigated domain D [19]:

$$E_{inc}\left(x_t, z_t, \omega, \underline{r}\right) = \frac{-\mu_o \omega}{2\pi} \int_{-\infty}^{+\infty} \frac{\exp\left\{-jk_{zb}(u) z\right\} \exp\left\{jk_{z0}(u) h_t\right\}}{\left[k_{zb}(u) + k_{z0}(u)\right]} \exp\left\{ju\left(x_t - x\right)\right\} du \qquad (3)$$

G(x_r, h_r, ω, $\underline{r}$) is the Green's function as expressed for the considered half-space reference scenario and accounts for the electric field at the receiving point (x_r, h_r) radiated by a point like target located in the generic point $\underline{r}$ of D [19]:

$$G\left(x_r, z_r, \omega, \underline{r}\right) = \frac{-j}{2\pi} \int_{-\infty}^{+\infty} \frac{\exp\left\{-jk_{zb}(v) z\right\} \exp\left\{jk_{z0}(v) h_r\right\}}{\left[k_{zb}(v) + k_{z0}(v)\right]} \exp\left\{jv\left(x_r - x\right)\right\} dv \qquad (4)$$

By using the expressions of the Green's function and of the incident field, eq. (2) can be rewritten in a spectral form as:

$$E_s\left(x_t, h_T, x_r, z_r, \omega\right) =$$

$$= \frac{j\omega\mu_0 k_b^2}{4\pi^2} \int_{-\infty}^{+\infty} \int_{-\infty}^{+\infty} \int_{-\infty}^{+\infty} \int_{-\infty}^{+\infty} \frac{\exp\left\{-j\left[k_{zb}(u) + k_{z0}(v)\right] z\right\} \exp\left\{ju\left(x_t - x\right) + v\left(x_r - x\right)\right\}}{\left[k_{zb}(u) + k_{z0}(u)\right]\left[k_{zb}(v) + k_{z0}(v)\right]} \times \qquad (5)$$

$$\exp\left\{k_{z0}(u) h_t + k_{z0}(v) h_r\right\} \chi(x, z)\, du\, dv\, dx\, dz = L[\chi]$$

Hence, the imaging is faced as the inverse problem to retrieve the contrast function starting from the scattered field data, i.e. as the inversion of operator L in eq.(5).

Once eq.(5) has been discretized into a linear algebraic system using the Method of Moments [24], the imaging is formulated as the solution of the matrix inversion problem:

$$\mathbf{E}_s = \mathbf{L}\boldsymbol{\chi} \qquad (6)$$

In eq.(6), $\mathbf{E}_s$ is the data vector made of $K = M \times F$ elements, where M represents the number of spatial measurement points and F is the number of working frequencies, $\boldsymbol{\chi}$ is the N-dimensional unknown vector, whose elements are the values of the contrast function at the centre of each one of the N pixels partitioning D, and $\mathbf{L}$ is the $K \times N$ matrix representing the discretized version of the integral operator in eq.(5).

The matrix inversion problem stated by eq.(6) is ill-conditioned and the Truncated Singular Value Decomposition (TSVD) approach [20] is adopted to gain a regularized solution as :

$$\tilde{\chi}(\underline{r}) = \sum_{n=1}^{T} \frac{\langle \mathbf{E}_s, \mathbf{u}_n \rangle}{\sigma_n} \mathbf{v}_n(\underline{r}) \tag{7}$$

In eq. (7), <·,·> denotes the scalar product in the data space, T is the truncation threshold, $\{\sigma_n\}_{n=1}^{\min\{K,N\}}$ is the set of singular values of the matrix $\mathbf{L}$ ordered in a decreasing way, $\{\mathbf{u}_n\}_{n=1}^{\min\{K,N\}}$ and $\{\mathbf{v}_n\}_{n=1}^{\min\{K,N\}}$ are the sets of the singular vectors, which are orthonormal bases in the data and unknown spaces, respectively [20]. The threshold $T \leq min\{K,N\}$ determines the “degree of regularization” of the solution and ensures the reliability of the result from being affected by errors/noise in the data. In practice, the choice of T is performed by accounting for the behaviour of the singular values of the matrix **L**and will be discussed in the following.

The imaging result is given as the spatial map of the modulus of the retrieved contrast vector normalized with respect to its maximum value. Hence, the regions of D where the modulus of $\tilde{\chi}$, as given by eq.(7), is significantly different from zero, give information on targets position and geometry.

III. Analysis of the Reconstruction Capabilities

In the frame of electromagnetic imaging, a crucial issue regards the analysis of the spatial resolution and, more in general, the quality of final image, which one can expect on the basis of the collected data (measurement configuration) and the level of noise and clutter. Answering to this question helps to give a reliable interpretation to the retrieved images as well as to drive a proper choice of the measurement configuration features, f.i. the scan length, the antennas height and the working frequency range.

Theoretical bounds, defining the spatial resolution in range and cross-range directions, are here evaluated for FLGPR configuration by resorting to a simplified ray-based model. As well known, in the case of multi-frequency data, the range resolution is well approximated by [11, 19, 25]:

$$\Delta R = \frac{c}{2B\sqrt{\varepsilon_b}} \tag{8}$$

where $B = f_{max} - f_{min}$ denotes the working bandwidth and c is the electromagnetic wave velocity in free space.

Accordingly, the range resolution mainly depends on the adopted frequency band, whereas it is weakly dependent on the target depth and the geometrical features of the measurement line, i.e. the scan extent and the antenna height.

On the other hand, following the reasoning given in [11, 19], we can expect that the cross-range resolution can be given as:

$$\Delta C_r = \frac{\lambda_{b,mean}}{2\sin(\theta_{view})} \tag{9}$$

where $\lambda_{b,mean}$ is the wavelength in the investigated soil at the mean frequency $f_{mean} = (f_{min} + f_{max})/2$ and θ_{view} is the maximum angle of view under which the target is probed. For the FLGPR case at hand, such an angle is defined as the difference between the

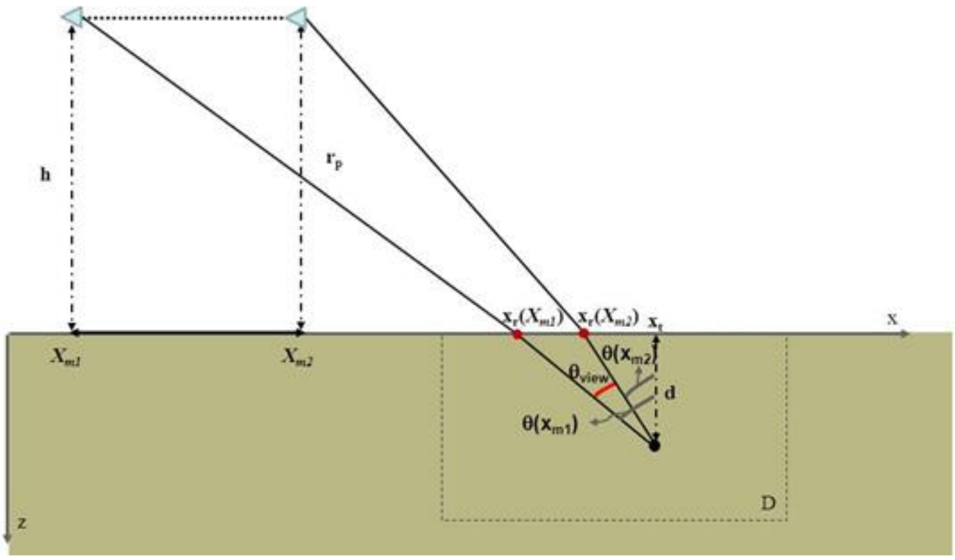

Fig.2 Sketch of wave propagation by using a ray based model

angles $\theta(X_{m1})$ and $\theta(X_{m2})$, as depicted in Fig.2. These latter are equal to the transmission angles as computed as in the reflection points, $(x_r(X_{m1}),0)$ and $(x_r(X_{m2}),0)$, corresponding to the starting and final positions of the antenna system [18], i.e. the extremes of the scan. It is worth observing that a physical constraint holds as dictated by the total reflection phenomenon and this entails that $\theta_{view} \in (0,\theta_c)$, $\theta_c = \sin^{-1}\left(\sqrt{\frac{1}{\varepsilon_b}}\right)$ being the critical angle [26]. Therefore, if the scan is long enough that $\theta(X_{m1}) \approx \theta_c$ and the target is sufficiently close to the end of the scan that $\theta(X_{m2}) \approx 0$, the cross range resolution reaches its best value $\Delta C_r^{Opt} = \lambda_{0,mean}/2$, $\lambda_{0,mean}$ being the wavelength in air at f_{mean}. Such a limit can be reached only in principle when the target is buried in a lossless media and if the length of the measurement line is sufficiently large.

The above observation leads to a criterion to choose the extent of the scanning line, for a given height h of the antennas and dielectric permittivity of the soil.

For sake of simplicity, let assume that a point target is located in the point $r_t = (0,d)$ in a medium whose relative permittivity is ε_b. For such a point, the best cross range resolution is reached, with a good approximation, when $\theta(X_{m1}) \approx \theta_c$, i.e., $x_r(X_{m1})$ approximates the abscissa $x_r(\theta_c,)$ of the reflection point corresponding to the critical angle, and when $\theta(X_{m2}) \approx 0$, i.e. $x_r(X_{m2})$ approaches to zero. It is worth noting that for the critical angle $x_r(\theta_c) = \frac{\sin(\theta_c)}{\sqrt{x_r^2(\theta_c) + d^2}}$ holds and this, after simple numerical manipulation, leads to $x_r(\theta_c) = d / \sqrt{\varepsilon_{b-1}}$.

Let α be a positive real number as low as it likes, the most convenient values of X_{m1} and X_{m2} are obtained by exploiting the Snell's law:

$$\frac{x_{ri} - X_{mi}}{\sqrt{(x_{ri} - X_{mi})^2 + \mathrm{h}^2}} = \sqrt{\varepsilon_b}\,\frac{x_{ri}}{\sqrt{x_{ri}{}^2 + \mathrm{h}^2}} \quad \text{with}\; x_{ri} = \begin{cases} d/\sqrt{\varepsilon_b - 1} - \alpha & i = 1 \\ \alpha & i = 2 \end{cases} \tag{10}$$

In particular, after numerical manipulation, the most convenient X_{m1} and X_{m2} are given by:

$$\begin{aligned} X_{m1}^{Opt} &= \max\left|\left(\frac{d}{\sqrt{\varepsilon_b - 1}} - \alpha\right)\left(1 \mp \sqrt{\frac{\varepsilon_b \mathrm{h}^2}{2\alpha \mathrm{d}\sqrt{\varepsilon_b - 1} - \alpha^2(\varepsilon_b - 1)}}\right)\right| \\ X_{m2}^{Opt} &= \min\left|\alpha\left(1 \mp \sqrt{\frac{\varepsilon_b \mathrm{h}^2}{\mathrm{d}^2 - \alpha^2(\varepsilon_b - 1)}}\right)\right| \end{aligned} \tag{11}$$

Equation (11) provides a general indication about the minimum and maximum distance that should occur between the target and the antenna system. Moreover, it allows us to correlate the extremes of the scan with the height of the antenna systems and the depth of the target to be imaged. Finally, it provides an upper limit for the standoff distance. In fact, if the standoff distance approaches to X_{m1} the cross resolution deteriorates dramatically becoming inadequate.

By removing the hypothesis of ray based model, the achievable reconstruction capabilities can be investigated by taking into account two figures as the spectral content (SC) [11, 19] of the object space and the regularized Point Spread Function (PSF) [11, 19, 20].

The spectral content is defined as the sum of the modulus of the discrete Fourier transform of the singular vectors $\underline{v}_n$ corresponding to the singular values that are above the (fixed) TSVD threshold T in eq.(7):

$$sp(\eta,\xi)=\sum_{n=1}^{T}\left|\hat{\underline{v}}_n(\eta,\xi)\right| \tag{12}$$

η and ξ being the spectral variables (conjugate variables with respect to x and z, respectively) and $\hat{\underline{v}}_n$ the 2D discrete Fourier's transform of $\underline{v}_n$:

$$\hat{\underline{v}}_n(\eta,\xi)=\sum_{x_i=1}^{N_x}\sum_{z_i=1}^{N_z}\underline{v}_n(x_i,z_i)e^{-j\eta x_i}e^{-j\xi z_i} \tag{13}$$

Once the scenario and the measurement configuration have been fixed, the spectral content gives an indication of the filtering effects introduced by the regularized inversion of the matrix **L**. Therefore, SC provides a global indication on the spatial harmonics of the targets that can be hopefully retrieved by using the TSVD for a fixed value of the regularization parameter. However, the spectral content does not give any information on how the reconstruction capability (resolution limits) varies with the actual location of the target inside the region under test.

This kind of information can be obtained by means of the regularized PSF [11, 19, 20], which is defined as the reconstruction of a point like target achieved by the TSVD regularization scheme. According to the TSVD scheme [20], the regularized PSF of an impulse located at (x_0, z_0) is given as function of the spatial variables (x, z):

$$\mathrm{PSF}(x,z,x_0,z_0)=\sum_{n=1}^{T}\underline{v}_n^{*}(x_0,z_0)\underline{v}_n(x,z) \tag{14}$$

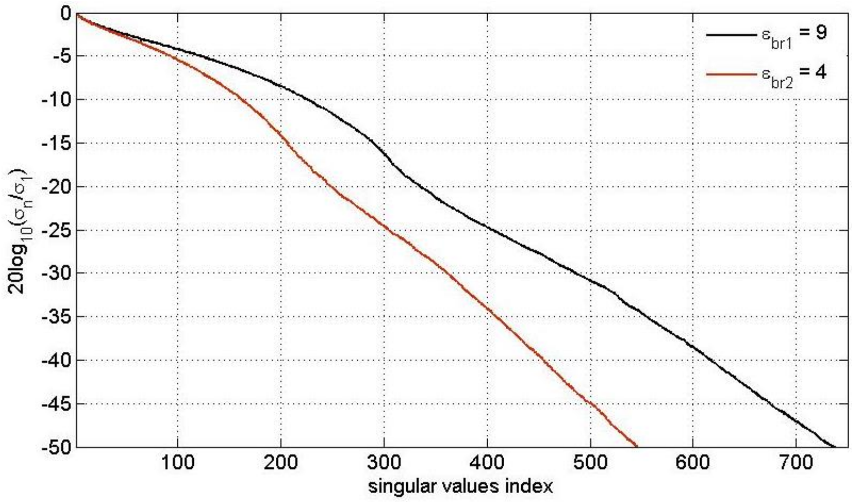

Fig.3 Singular Values behavior for three different soils.

* being the conjugation operation.

Let us turn now to a numerical/theoretical analysis for two examples.

With respect to the reference system given in Fig.1, let us assume the investigated domain has extent [5, 8] m along x-axis and [0, 1.7] m along z-axis. The antenna system is moved along x-axis from 0.25 m to 4.75 m with a spatial step Δx_m = 0.1 m and the height of the transmitting and receiving antennas are h_t = 3.5 m and h_r = 4.5 m, respectively. The data are gathered in the frequency range [0.4 - 1.3] GHz with a frequency step Δf = 11 MHz. The two cases differ for the dielectric relative permittivity of the background medium that is ε_{br1} = 9 and ε_{br2} = 4, respectively.

Figure 3 shows the behaviour of the singular values of the matrix **L** for the two cases (ε_{br1} = 9 and ε_{br2} = 4). The curves in Fig.3 show a change of the slope behaviour in the range from -20 dB to -15 dB and suggest to set the TSVD threshold T in such a way to consider the singular vectors corresponding to the singular values no lower than -15 dB with respect to the maximum one, i.e. T = 290 for ε_{br1} = 9 and T = 207 for ε_{br2} = 4.

With respect to these threshold values, the spectral contents, as computed from eq.(12) and normalized to their own maximum value, are shown in Figs.4a,b. According to the results provided in [11], Fig.4 shows that, due to the limited angle

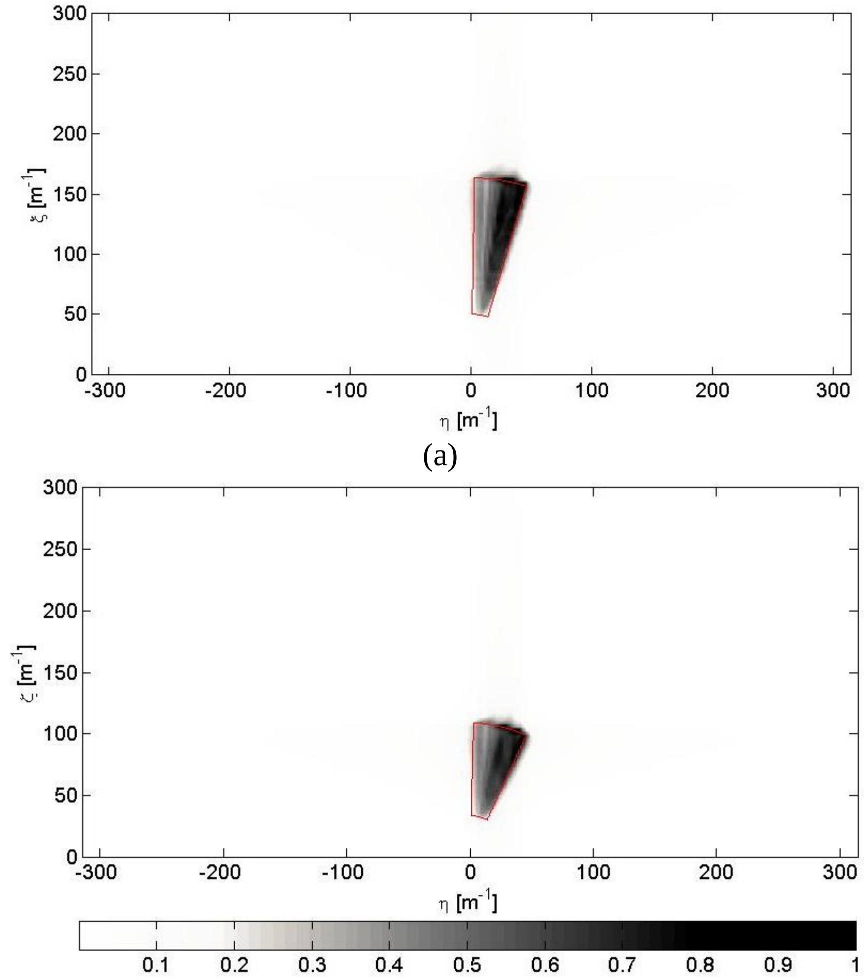

(a)

(b)

Fig.4 Spectral content: a) soil having relative permittivity equal to 9; b) soil having relative permittivity equal to 4. The red contour represents the portion of the plane (η, ξ) bounded by the arcs of two half-circumferences centred at (0,0) and having radius $2k_{b\min}$ and $2k_{b\max}$ and it is limited by two radial segments, which are described by the points $(2k_b\cos\theta(X_{mi}), 2k_b\sin\theta(X_{mi}))$

under which the investigated domain is probed, the retrievable spectral content is significant only in a limited area of the spectral plane (η, ξ). This area is well approximated by the portion of the plane (η, ξ) bounded by the arcs of two half-circumferences centred at (0,0) and having radius $2k_{b\min}$ and $2k_{b\max}$, being $k_{b\min}$ and $k_{b\max}$ the wave number in the probed soils at the minimum and maximum working frequencies. Moreover, the covered area is limited by two radial segments, which are described by the points $(2k_b\cos\theta(X_{mi}), 2k_b\sin\theta(X_{mi}))$, with $i = 1, 2$ and k_b ranging from

$k_{b\min}$ to $k_{b\max}$. The value of the angles are $\theta(X_{m1}) = 0.29$ rad and $\theta(X_{m2}) = 0.02$ rad for $\varepsilon_{br1} = 9$, $\theta(X_{m1}) = 0.43$ rad and $\theta(X_{m2}) = 0.03$ for $\varepsilon_{br2} = 4$.

This result corroborates that, if a forward looking measurement configuration is adopted, the regularized inversion of the matrix **L** acts as a band pass spatial filter in the range and as a low-pass filter in cross-range direction, analogously to the case of the down looking radar. In particular, while the filtering effect along the range direction depends mostly on the working frequency range and the relative permittivity of the soil, the filtering effect arising along the cross-range direction is strongly dependent on the angle of view. Accordingly, the same range resolution is expected whatever is the target position; differently, the cross-range resolution is strongly dependent on the relative position of the scanning line with respect to the target position. This is confirmed by Figs.5a-c and Figs.6a-c, which show, for the considered soils, the regularized PSF as computed for points located at growing distances from the measurement line but at a constant depth d = 0.85 m.

In particular, Figs.5, 6 depict the quantity given by:

$$\mathrm{PSF}(x,z,x_0,z_0) = 20\log_{10}\left[\frac{\left|\sum_{n=1}^{T}\underline{v}_n^*(x_0,z_0)\underline{v}_n(x,z)\right|}{\max\limits_{(x,z)\in D}\left|\sum_{n=1}^{T}\underline{v}_n^*(x_0,z_0)\underline{v}_n(x,z)\right|}\right]. \qquad (15)$$

From these figures, the numerical values of the range and cross-range resolution in each one of the considered points can be numerically estimated. The numerical estimation of the resolution limits is performed by evaluating the width of the main lobe at the points at 0.5 times the maximum of the main lobe (i.e. at -6 dB by defining the PSF as in eq.(15)). Tables I compares the resolution limits numerically evaluated with the theoretical ones provided by eq.(8) and eq.(9). Table I allows us to state that

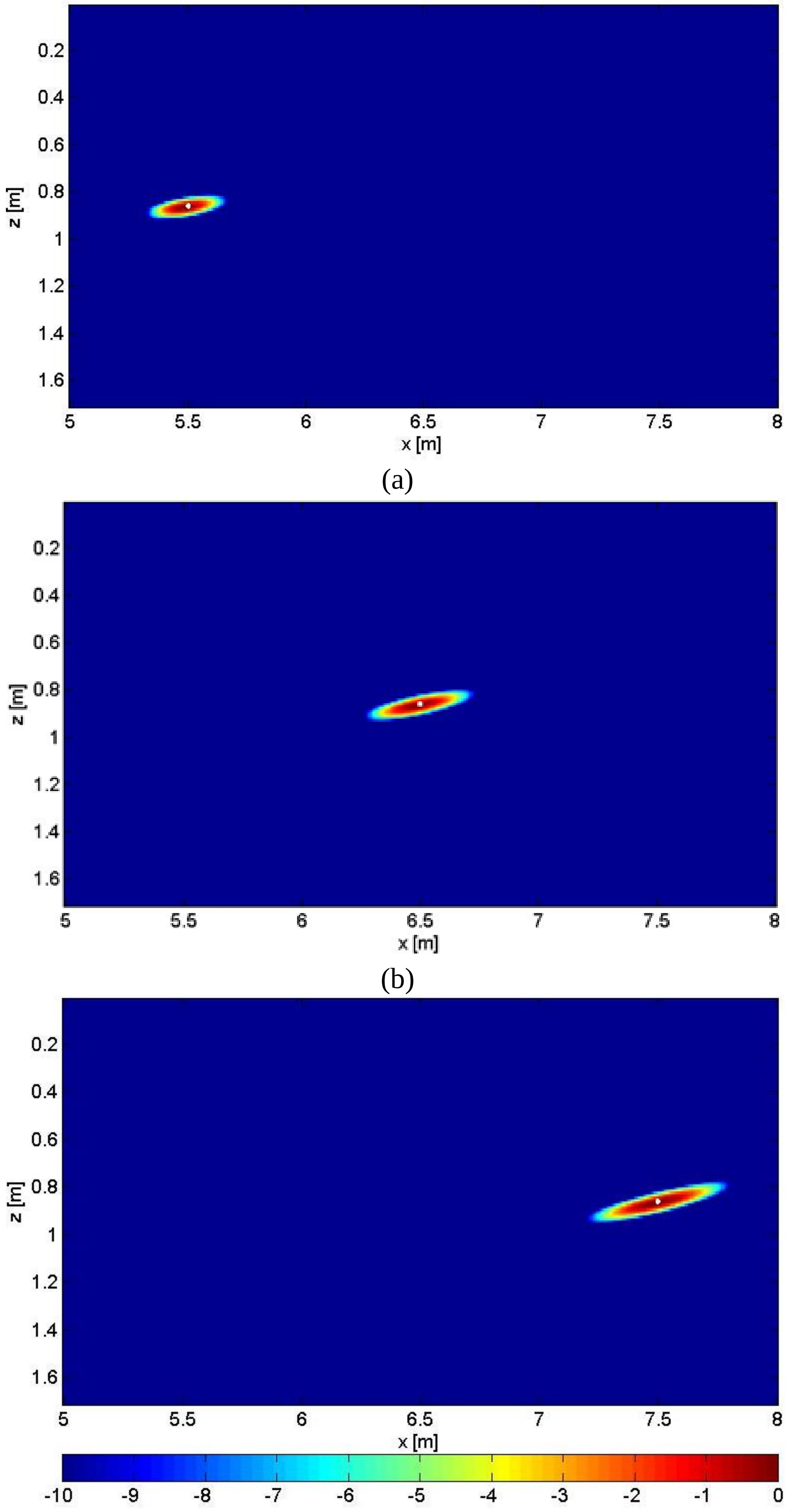

(a)

(b)

(c)

Fig.5 PSF corresponding to 3 points located at growing distances from the measurement line but at the same depth d = 0.85m in a soil having relative permittivity ε_{br1} = 9: a) x_t=5.5m; b =6.5m; c) x_t=7.5m.

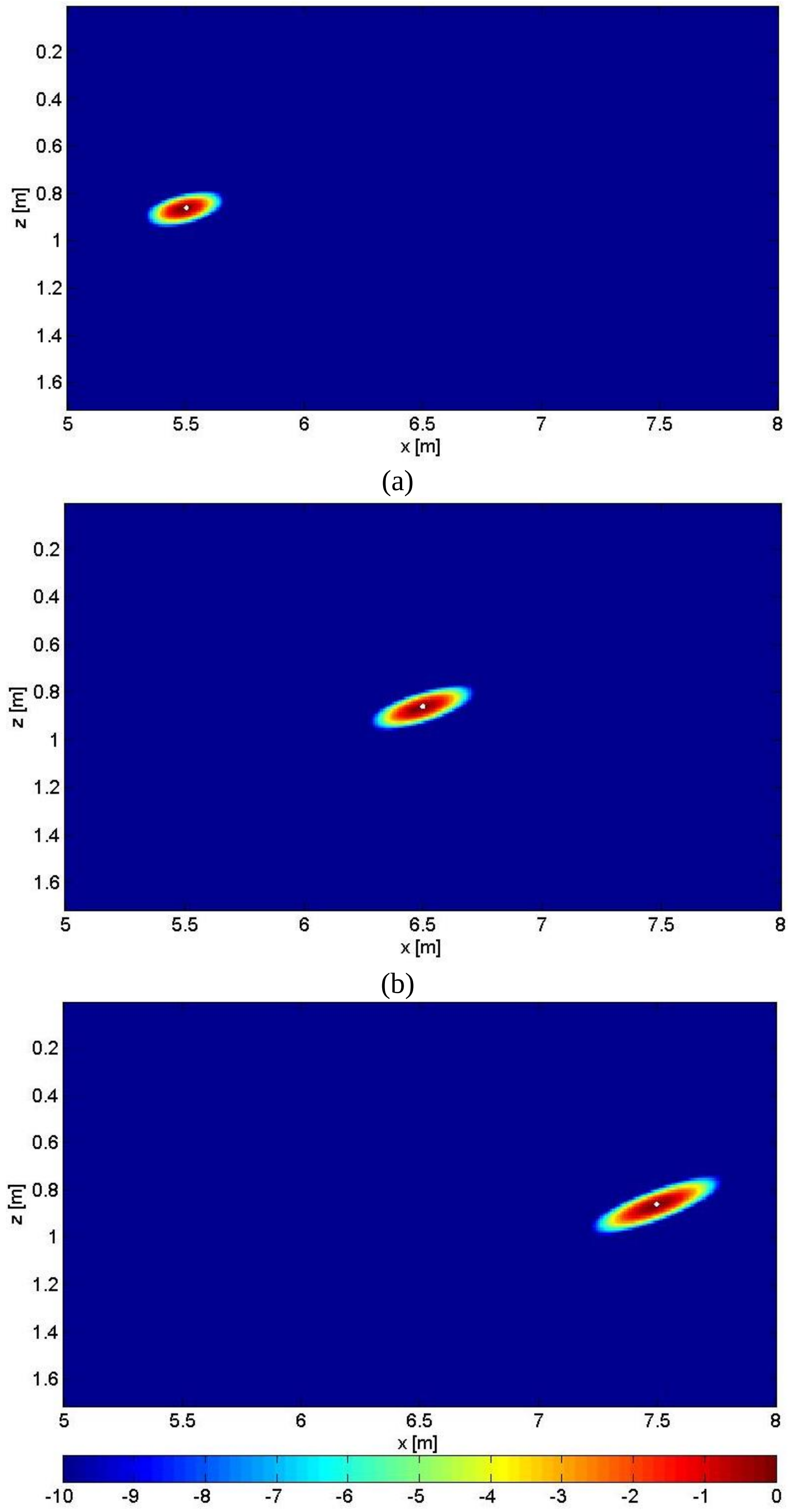

(a)

(b)

(c)

Fig.6 PSF corresponding to 3 points located at growing distances from the measurement line but at the same depth d = 0.85m in a soil having relative permittivity $\varepsilon_{br1} = 4$: a) x_t=5.5m; b =6.5m; c) x_t=7.5m.

Table I: range and cross range resolution values in meters

	$\varepsilon_{br1} = 9$				$\varepsilon_{br2} = 4$			
	Numerical		Theoretical		Numerical		Theoretical	
x_t	ΔR	ΔC_r	ΔR	ΔC_r	ΔR	ΔC_r	ΔR	ΔC_r
5.5 m	0.08	0.30	0.06	0.30	0.11	0.30	0.08	0.30
6.0 m	0.08	0.33	0.06	0.33	0.11	0.33	0.08	0.33
6.5 m	0.08	0.38	0.06	0.38	0.11	0.37	0.08	0.37
7.0 m	0.08	0.44	0.06	0.44	0.11	0.42	0.08	0.42
7.5 m	0.08	0.51	0.06	0.51	0.11	0.48	0.08	0.48

there is a good agreement among the numerical and theoretical spatial resolution values for both the cases.

IV. *Imaging results*

A. Numerical Assessment: 2D scalar case

A first assessment of the reconstruction capabilities of the inversion approach is herein provided by processing synthetic data. These data have been generated in the time domain by using GPRMax 2D, which is a free GPR modelling code based on Finite Difference Time Domain (FDTD) technique [27]. The targets are supposed to be buried in a soil with $\varepsilon_{br} = 9$ and $\sigma_b = 10$ mS/m, which is probed by the same multi-bistatic measurement configuration described in Section III. Hence, the transmitting antenna is at height $h_t = 3.5$ m and the receiving one at $h_r = 4.5$ m from the air-soil interface and the antennas are moved jointly with a spatial step $\Delta x_m = 0.1$ m along a scan going from $X_{m1} = 0.25$ m to $X_{m2} = 4.75$ m. The transmitting antenna assumes as source's excitation waveform a Ricker wavelet, whose central frequency is 600 MHz. The effective frequency range of the data is from 400 MHz to 1300 MHz and is sampled by means of 82 frequencies. The domain under test ranges from 5 m to 8 m along the x - axis and from 0 m to 1.7 m along the z – axis.

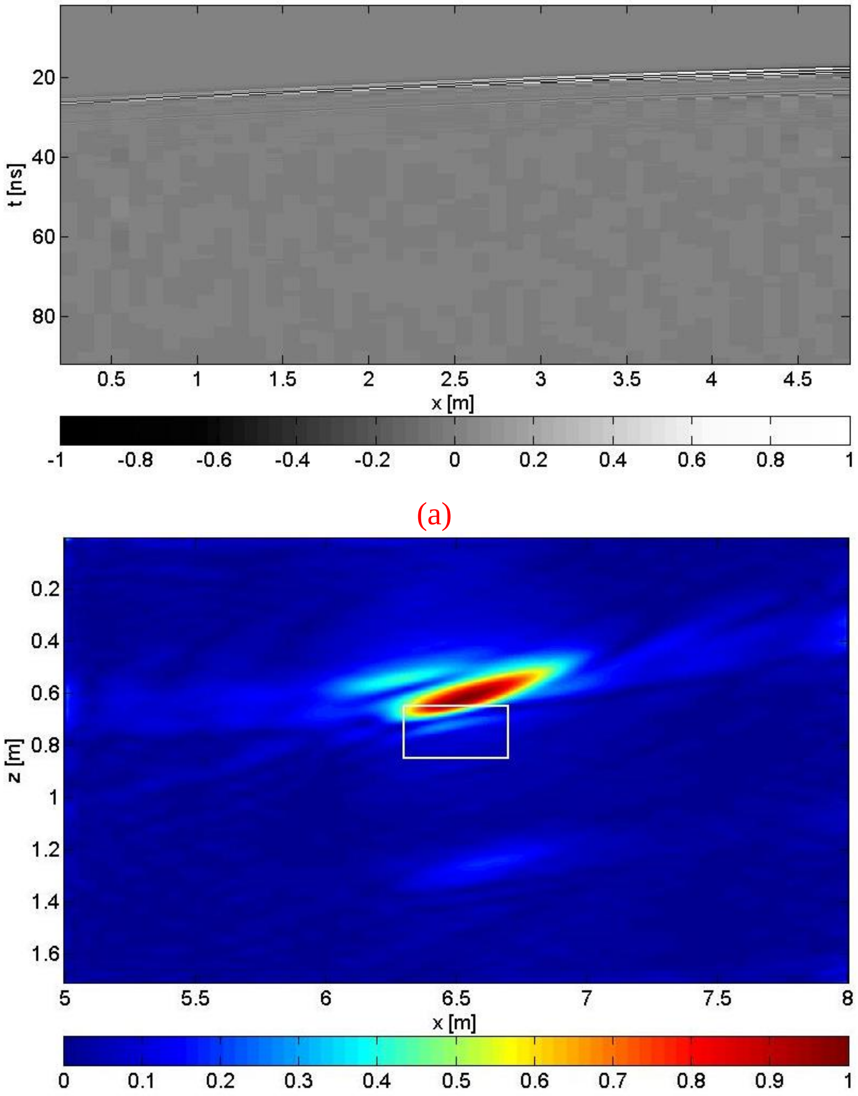

(a)

(b)

Fig.7 Example 1: a) GPRMax2D simulated backscattered field engendered by the target; b) tomographic reconstruction (T = 290), the white contour represents the cavity to be imaged.

The first example concerns a single 0.40 m x 0.20 m void located at the centre of the investigated domain. Noiseless scattered field data are shown in Fig.7a. Such a scattered field is obtained as the subtraction of the total field (in presence of the target) and the background field (in absence of the target).

Figure 7b shows the tomographic reconstruction obtained by setting the TSVD threshold in such a way to filter out the singular vectors corresponding to the singular values lower than -15 dB with respect to the maximum one, i.e. *T* = 290.

Although this first example deals with an ideal (noise free) dataset, it is worth of consideration because it states what kind of images one should expect when the approach proposed in Section II is adopted. In particular, Fig.7b assesses that the proposed approach is capable of providing an accurate localization of the upper face of the target and an approximate estimation of its depth.

As a second example, let us consider two 0.40 m x 0.20 m voids centred in (6.30 m, 0.75 m) and (7.20 m, 0.75 m), with respect to the reference system introduced in Fig.1. In this case, the total field simulated by means of GPRMax 2D has been corrupted by an additive Gaussian noise with a Signal to Noise Ratio of 45 dB and has been directly processed. This means that the scattered field has been achieved directly from the total field by using a filtering procedure consisting of time gating plus background removal, with the aim to remove the signal contributions due to the antennas coupling and the air-soil interface.

The tomographic reconstruction is depicted in Fig.8. Since the processed data are affected by noise, in the case at hand the TSVD threshold has been set in such a way to consider only the singular vectors corresponding to the singular values higher than -10 dB with respect to the maximum one, i.e. $T = 226$.

The accuracy of the tomographic reconstruction shown in Fig. 8 looks like that of Fig.7b, which has been obtained by processing ideal noiseless data. Therefore, this second example corroborates the ability of the proposed approach to retrieve correctly the targets location along the *x*-axis as well as to provide a rough estimation of their depth even in the case of noisy total field data. Moreover, as it is suggested by the resolution analysis given in Section III, one can observe a slight loss of the cross-range resolution for the most distant target, whose reconstruction is also affected by a

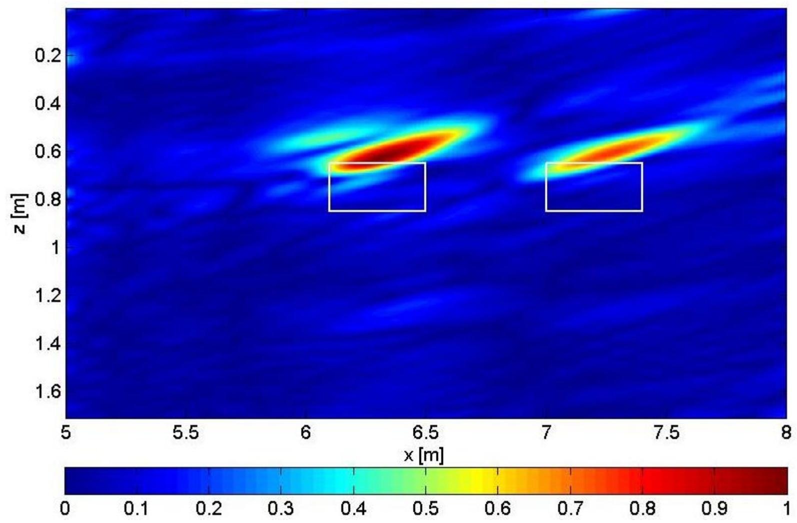

Fig.8: Example 2 - tomographic reconstruction (T = 226), the white contours represent the cavities to be imaged.

slight masking effect due to the presence of the target centred in (6.30 m, 0.75 m).

As a third example, the two above considered voids have been supposed to be hidden in an inhomogeneous medium made by three layers and four materials all having σ_b = 10 mS/m (see Fig.9a). In particular, the first layer is 0.30 m thick and has ε_{br1} = 9, the second layer is 0.70 m thick and is made by two different materials having ε_{br2a} = 8.5 and ε_{br2b} = 9.5, respectively, the third layer is a half-space having ε_{br3} = 12. The inhomogeneity of the probed medium has been neglected in the imaging approach, wherein the reference scenario has been modelled as an half space made by air (upper part) and a homogeneous soil (bottom part) having ε_{br} = 9. The data have been gathered under the above described measurement configuration and corrupted by an additive Gaussian noise with a Signal to Noise Ratio of 45 dB. The tomographic reconstruction is given in Fig.9b and has been obtained by setting the TSVD as in the previous example, i.e. T = 226. Such a result is promising since it suggests that the approach is sufficiently robust against uncertainties on the investigated medium.

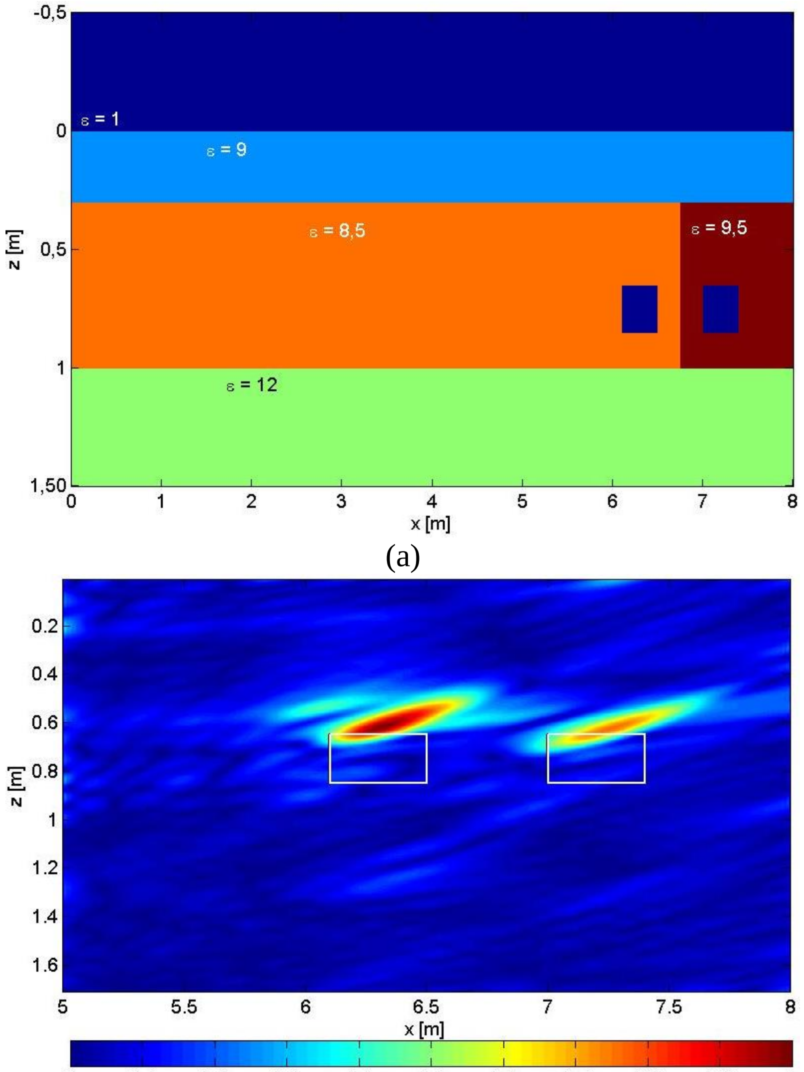

(a)

(b)

Fig.9: Example 3: a) reference scenario; b) tomographic reconstruction (T = 226), the white contours represent the cavities to be imaged.

B. Numerical Assessment: 3D case

In this subsection, the reconstruction capabilities of the 2D proposed approach have been validated against a synthetic dataset relative to a full 3D scenario, which has been simulated by using GPRMax 3D code.

The probed scenario is made by two targets buried in a soil having $\varepsilon_{br} = 9$ and $\sigma_b =$ 1mS/m. Both the targets are 0.04 m long in the *z*-direction and have a circular cross section in the (*x*,*y*) plane. One target has radius equal to 0.035 m, relative permittivity

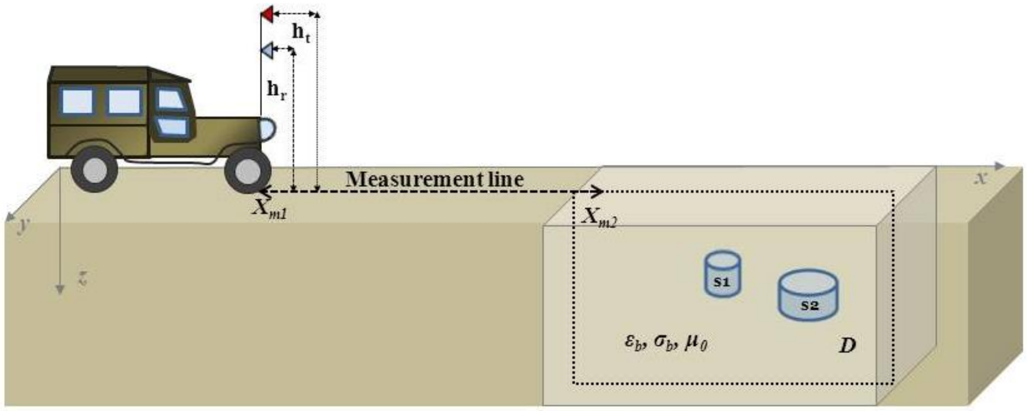

Fig.10 Full 3D scenario

ε_{t1} = 2.3 and is centred at the point $\boldsymbol{r}_{t1}$=(4.0m, 0.25m, 0.12m), the other target has radius equal to 0.06 m, ε_{t2} = 2.7 and it is centred at $\boldsymbol{r}_{t2}$=(4.5m, 0.25m, 0.17m).

The transmitting antenna is at height h_t = 1 m and the receiving one at h_r = 2 m from the air-soil interface and are moved with a spatial step Δx_m = 0.03 m along a scan at y = 0.25m and ranging from X_{m1}= 0.25 m to X_{m2}= 3 m, with respect to the coordinate system introduced in Fig.10. The transmitting antenna is fed by a Ricker wavelet, whose central frequency is 600MHz and the synthetic radargram (representing the total field) has been corrupted by an additive Gaussian noise, by leading to a Signal to Noise Ratio of 45 dB. The effective frequency range of the data is from 400MHz to 1300MHz and has been sampled by means of 46 frequencies. The investigated domain ranges from 2.5 m to 5.5 m along the x - axis and from 0 m to 0.5 m along the z – axis.

The tomographic reconstruction obtained by assuming exactly known the relative permittivity of the soil is given in Fig.11a, while Figs.11b,c show the reconstructions obtained by assuming a wrong value of soil permittivity, i.e. ε_{br} = 4, and that achieved by assuming a free space reference scenario, as it has been made in [17], respectively. The reconstructions have been obtained by setting the TSVD threshold in such a way to filter out the singular values lower than -10 dB with respect to the maximum one.

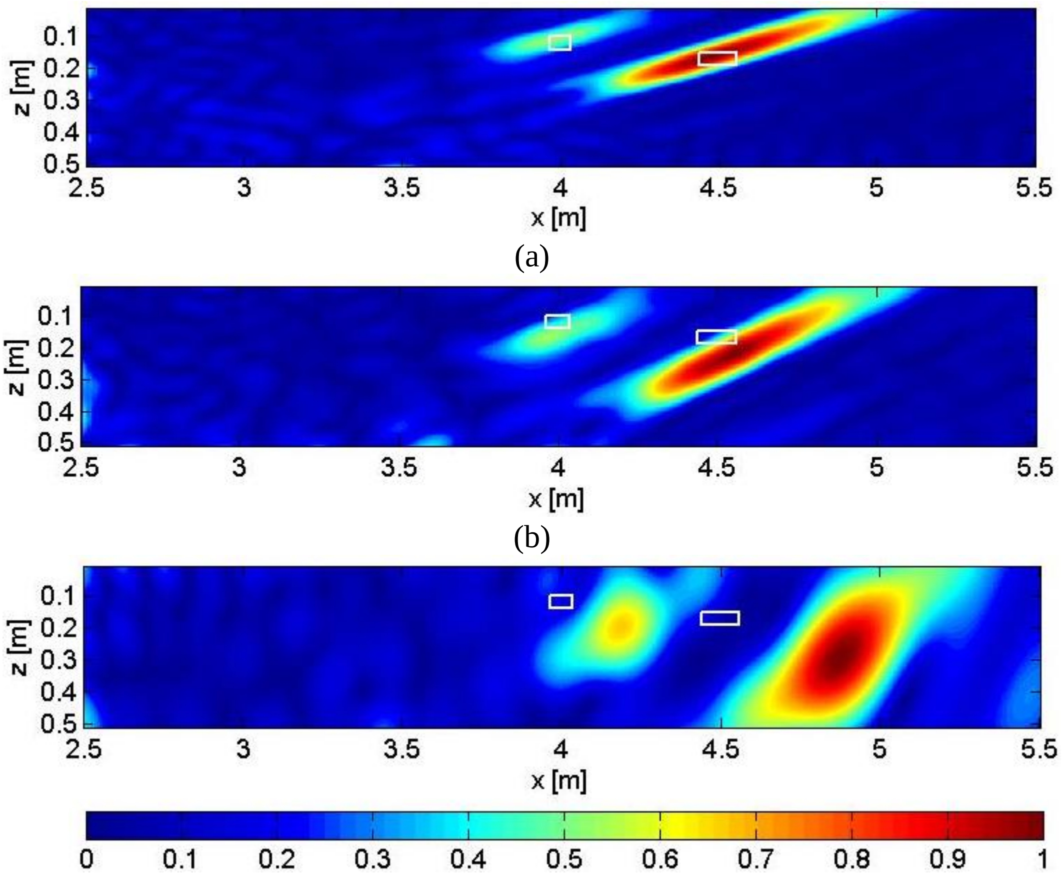

(a)

(b)

(c)

Fig.11: Example 4 - tomographic reconstructions: a) exactly known soil permittivity; b) wrong soil permittivity; c) free space reference scenario. The white contour represent x-z slice of the actual targets.

These results validate the capability of the approach to properly image both the targets even if, as expected, the cross resolution becomes worse when the distance between the scanning line and the target increases. Moreover, one can observe that the use of a not exact value of ε_{br} mainly implies a spatial shift of the reconstructed targets location with respect to their actual position, which increases with the error on the soil permittivity. This behaviour is the same of that observed in [28] in the frame of down looking data. In addition, the reconstructions in Figs.11b,c are affected by a worsening of range and cross-range resolutions, which is due to the fact that the maximum wave number assumed in the inversion procedures decreases since a wrong soil dielectric permittivity equal to $\varepsilon_{br} = 4$ or $\varepsilon_{br} = 1$, instead of $\varepsilon_{br} = 9$, are considered.

Table II: range and cross range resolution values in meters

	$\varepsilon_{br1} = 9$				$\varepsilon_{br2} = 4$				$\varepsilon_{br3} = 1$			
x_t	Numerical		Theoretical		Numerical		Theoretical		Numerical		Theoretica	
	ΔR	ΔC_r	ΔR	ΔC_r	ΔR	ΔC_r	ΔR	ΔC_r	ΔR	ΔC_r	ΔR	ΔC_r
4.0 m	0.12	0.46	0.06	0.39	0.14	0.44	0.08	0.37	0.24	0.35	0.17	0.31
4.5 m	0.12	0.70	0.06	0.54	0.14	0.63	0.08	0.51	0.24	0.42	0.17	0.37

To support this observation, the theoretical and the numerical range and cross-range resolutions, as computed for the measurement configuration and investigated domain herein considered at the central point of the targets, are given in Table II. In this case, the numerical resolution values have been obtained by computing the PSF according to eq.(14) and setting the TSVD threshold in such a way to filter out all the singular values lower than -10dB with respect to the maximum one, i.e. the threshold value used to obtain the tomographic reconstructions depicted in Figs.13a-c. Compared to Table I, the smaller value of the TSVD threshold (-10 dB instead of -15 dB), results in a large degree of regularization and accordingly entails a loss of the actual achievable range and cross range resolutions.

Finally, it is worth noting that the use of the free space reference scenario although allows the target detection implies a significant worsening of the imaging result in terms of localization and geometry estimation of the targets.

C. Experimental Assessment

A first test of the achievable performance in realistic conditions has been performed by processing experimental data collected by using the test facilities available at IDS – Ingegneria dei Sistemi S.p.a. headquarter, where a test site made by a number of consecutive cells containing different kind of soils is available, see Figs.12a,b.

The data have been gathered in the frequency range 0.4 – 2 GHz by using two ridge horn antennas connected to a network analyser. The antenna have been 45° tilted, 93.5 cm spaced one to the other one and mounted on a moving platform 1.42 m far from the air-soil interface, see Fig.12a. The platform has been moved along straight tracks with a spatial step of 0.02 m and a scan about 8 m long has been performed.

The data have been collected on the sandy portion of the test site, which although simple is far from a laboratory scenario. In particular, due to the rain falls occurred few days before the experiment, the probed medium (sand scenario) is not homogeneous but can be seen as a two layer structure, wherein the upper layer, about a few centimeters thick, is made by dry sand while the deeper layer is wet sand. This clearly appears in Figs.12c,d that show two buried targets, i.e. a metallic plate and a plastic tank. Moreover, from Fig.12 one can observe that the air soil interface is not perfectly flat and there are several clutter sources, among which the metallic structure where the antennas are mounted and the metallic rails used to move the structure along the test site.

Several targets have been buried in the probed sandy soil previously to the measurement campaign, and several targets are not centred with respect to the middle point between the antennas, which has been taken as the scan location in the imaging approach. It is worth mentioning that, since the antenna have been mounted at the same height from the air-soil interface, the data have been processed by assuming the transmitter and the receiver located at the same points. The relative dielectric permittivity of the sand has been set as $\varepsilon_{br} = 4$.

The raw radargram (i.e. the total field), the filtered one provided by the filtering procedure introduced in section IV.A and the tomographic reconstruction are given in Figs13a-c. It is worth mentioning that, for the case at hand, we observed that the

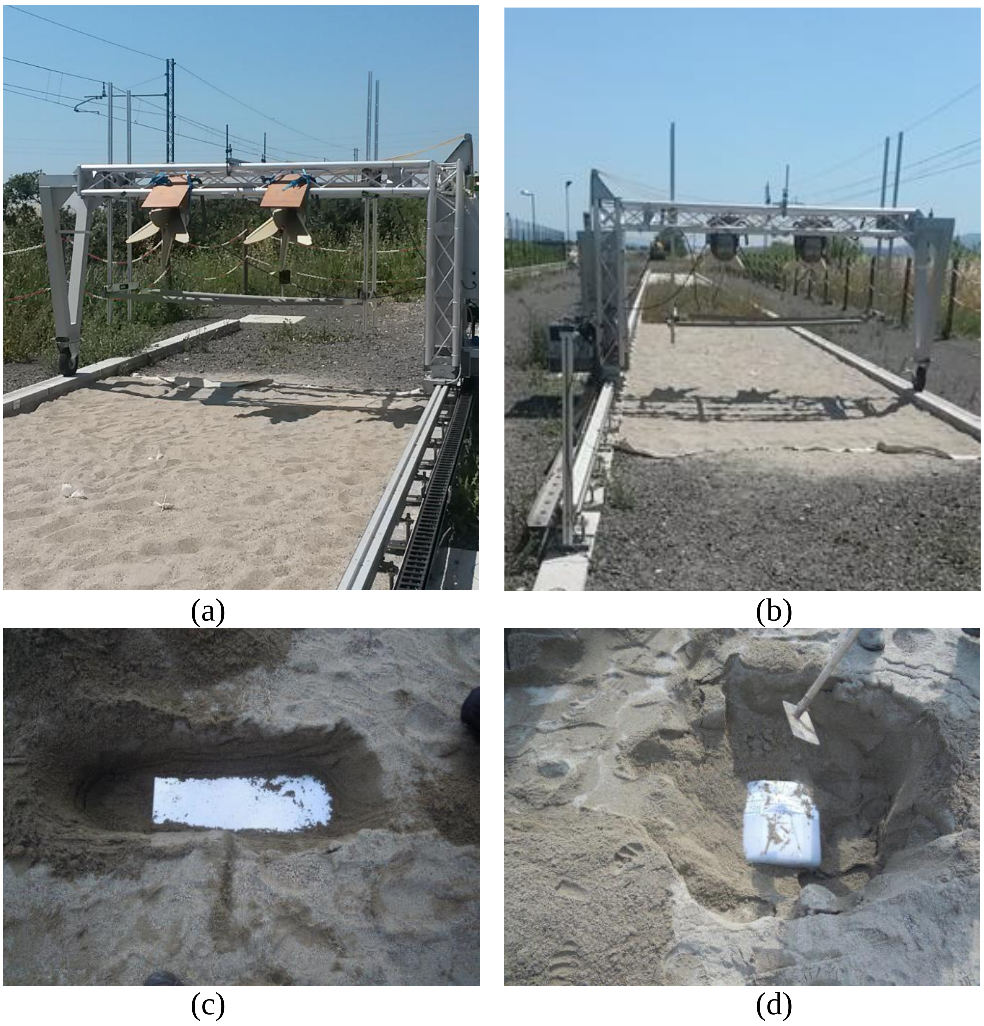
(a) (b)

(c) (d)

Fig.12 Experimental test site: a) front view; b) back view; c) metallic plate target; d) plastic tank target.

useful signal occurred in a time window about 10 ns width and Figs.13a,b have been constrained to this time window.

Figure 13c has been obtained by sampling the working frequency range with a step of 80MHz, which agrees with the Nyquist-Shennon criterion and the rule given in [29], being the maximum investigated distance equal to 0.75 m (resulting from the adoption of the time window of 10 ns for the data), and by setting the TSVD threshold in such a way to filter out all the singular values lower than -5 dB with respect to the maximum one. This TSVD threshold was adopted due to the high environmental noise affecting the data. Figure 13 supports the ability of the considered approach to provide a focused image of the probed scenario from which it is possible to localize

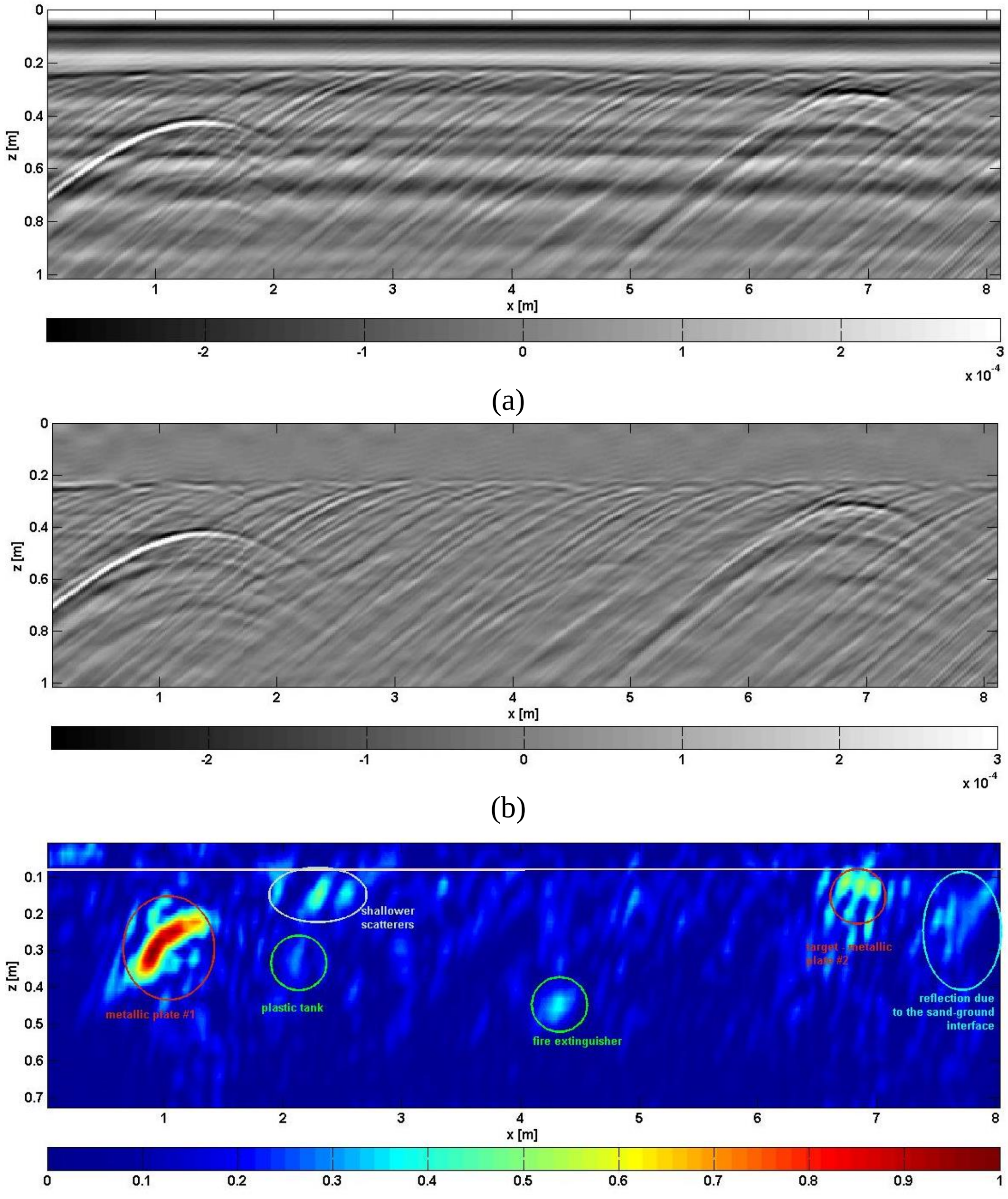

(a)

(b)

(c)

Fig.13 Experimental assessment: a) raw radargramm; b) filtered radargramm; c) tomographic reconstruction.

the targets hidden in the experimental test site. In particular, the metallic plates, which were centered with respect to the scan, are clearly imaged as well as the interface between the sand and the ground occurring at the end of the probed scenario. Moreover, since a 2D scattering model is adopted, targets located on the left and right sides of the scan, such as the plastic tank and the fire extinguisher are also imaged into the investigation domain.

V. *Conclusions*

A microwave tomography approach to image buried targets under a forward looking measurement configuration has been proposed. Such an approach has been formulated with respect to the canonical 2D scalar case and exploits a Born Approximation based scattering model accounting for the presence of a flat air-soil interface. The imaging capabilities of the approach in terms of range and cross range resolution limits have been discussed and verified against synthetic and experimental noisy data, accounting for homogeneous and inhomogeneous scenarios.

Future works will be addressed to further investigate the performance of the approach in field conditions as well as to extend it in order to account for the actual radiation pattern of the adopted antenna system. An initial step in this latter direction has been already made in the frame of down-looking GPR systems [30, 31]. In addition, the approach will be modified to process multi-input multi-output data gathered by means of array antenna based systems and will be reformulated by assuming a full 3D scattering model. Finally, the development of target identification strategies able to assure a low false alarm rate will be taken into account.

REFERENCES

[1] J. Kositsky, R. Cosgrove, C. A. Amazeen, P. Milanfar: “Results from a forward-looking GPR mine detection system”. *Proc. SPIE Detection and Remediation Technologies for Mines and Minelike Targets* VII, vol.4742, pp.206-217, Aug. 2002.

[2] M. R. Bradley, T. R. Witten, M. Duncan, R. McCummins, “Anti-tank and side-attack mine detection with a forward-looking GPR”, *Proc. SPIE Detection and Remediation Technologies for Mines and Minelike Targets* IX, vol.5415,p p. 421-432, Sept. 2004.

[3] T. Wang, O. Sjahputera, J. M. Keller, P. D. Gader, “Landmine detection using forward-looking GPR with object tracking”, *Proc. SPIE Detection and Remediation Technologies for Mines and Minelike Targets* X, vol.5794, pp. 1080-1088, July 2005.

[4] F. Soldovieri, I. Catapano, “Close Sensing Radar Systems enhanced by Microwave Tomography for IED detection and localization”, *Proc. Resilient Threat Management - IEDs and Beyond*, pp.40-44, Mar 2013.

[5] Y. Sun, J. Li, “Time–frequency analysis for plastic landmine detection via forward-looking ground penetrating radar”, *IEE Proc. - Radar, Sonar and Navigation*, vol.150 (4), pp. 253-261, Aug. 2003.

[6] Y. Wang; Y. Sun; J. Li; P. Stoica, “Adaptive imaging for forward-looking ground penetrating radar", *IEEE Trans. on Aerospace and Electronic Systems*, vol.41 (3), pp.922-936, July 2005.

[7] T. Wang, J. M. Keller, P. D. Gader, O. Sjahputera, "Frequency Sub-band Processing and Feature Analysis of Forward-Looking Ground-Penetrating Radar Signals for Land-Mine Detection," *IEEE Trans. on Geosci. and Remote Sens*., vol.45 (3), pp.718,729, Mar. 2007.

[8] Hyoung-sun Youn; J. Kobashigawa, M. Evans, N. Celik, Y. Zhengqing; J. Baker, M. Iskander, "Feasibility study for IED detection using forward-looking ground penetrating radar integrated with target features classification", *Proc. IEEE Antennas and Propag. Society Int. Symposium* (APSURSI), 4 pp., July 2010.

[9] T. Ton; D. Wong, M. Soumekh, "ALARIC Forward-Looking Ground Penetrating Radar system with standoff capability", *Proc- IEEE Int. Conf. on Wireless Information Technology and Systems* (ICWITS), 4 pp., Sept. 2010.

[10] J. Farrell, T. C. Havens, K. C. Ho, J. M. Keller, T. T. Ton, D. C. Wong, M. Soumekh, “Detection of explosive hazards using spectrum features from forward-looking ground

penetrating radar imagery”, *Proc. SPIE Detection and Sensing of Mines, Explosive Objects and Obscured Targets* XVI, vol. 8017, May 2011.

[11] I. Catapano, F. Soldovieri, M.A. González-Huici, “Performance assessment of a microwave tomographic approach for the Forward Looking Radar configuration”, *Sens. Imaging,* vol.91 (1), 13 pp, Apr. 2014.

[12] B.R. Phelan, K.D. Sherbondy, K.I. Ranney, R.M. Narayanan, “Design and performance of an ultra-wideband stepped-frequency radar with precise frequency control for landmine and IED detection”, *Proc. SPIE Radar Sensor Technology* XVIII, vol.9077, 12 pp. May 2014.

[13] J. Yang, T. Jin, X. Huang, J. Thompson, Z. Zhou, "Sparse MIMO Array Forward-Looking GPR Imaging Based on Compressed Sensing in Clutter Environment", *IEEE Trans. on Geosci. and Remote Sens*., vol.52 (7), pp.4480-4494, July 2014.

[14] F. Soldovieri, J. Hugenschmidt, R. Persico, G. Leone, “A linear inverse scattering algorithm for realistic GPR applications”, *Near Surface Geophys.*, vol.5 (1), pp.29–42, 2007.

[15] G. Leucci, R. Persico, F. Soldovieri, "Detection of fractures from GPR data: the case history of the Cathedral of Otranto”, *J. Geophys. Eng*. vol.4, pp.452–61, Oct. 2007.

[16] F. Soldovieri, O., Lopera, S. Lambot, “Combination of advanced inversion techniques for an accurate target localization via GPR for demining applications”, *IEEE Trans. on Geosci. and Remote Sens.*, vol.49 (1), pp.451–461, Jan. 2011.

[17] I. Catapano, L. Crocco, R. Di Napoli, F. Soldovieri, A. Brancaccio, F. Pesando, A. Aiello, “Microwave tomography enhanced GPR surveys in Centaur’s Domus, Regio VI of Pompeii, Italy”, *J. Geophys. Eng*. vol.9, pp-S92–S999, Aug. 2012.

[18] I. Catapano, L. Crocco, G. Triltzsch, Y. Krellmann, F. Soldovieri, “A tomographic approach for helicopter-borne ground penetrating radar imaging”, *IEEE Geosci. and Remote. Sens. Letters.*, vol.9 (3), pp.378–382, May 2012.

[19] R. Persico, *Introduction to ground penetrating radar: inverse scattering and data processing*, IEEE Press Series on Electromagnetic Wave Theory”. New York: Wiley, 2014.

[20] M. Bertero, "Linear inverse and ill-posed problems," Adv. in Electron. and Electron. Phys., vol.45, pp. 1-120, 1989.

[21] F. Soldovieri, R. Solimene, "Through-Wall Imaging via a Linear Inverse Scattering Algorithm," *IEEE Geosci and Remote Sens. Letters*, vol.4 (4), pp.513-517, Oct. 2007.

[22] E. Pettinelli, A. Di Matteo, E. Mattei, L. Crocco, F. Soldovieri, J.D. Redman, A.P. Annan, "GPR Response From Buried Pipes: Measurement on Field Site and Tomographic Reconstructions," *IEEE Trans on Geosci. and Remote Sens.*, vol.47 (8), pp.2639-2645, Aug. 2009.

[23] G. Gennarelli, F. Soldovieri, "Multipath Ghosts in Radar Imaging: Physical Insight and Mitigation Strategies", *IEEE J. Selected Topics in Applied Earth Obs. and Remote Sen*s.,vol.8 (3), pp.1078-1086, Mar. 2015.

[24] R. F. Harrington, *Field Computation by Moment Methods*, IEEE Press Series on Electromagnetic Waves, 1993.

[25] H. M. Jol, *Ground Penetrating Radar Theory And Applications*, Elsevier, 2009.

[26] C. A. Balanis, *Advanced Engineering Electromagnetics*, John Wiley & Sons, Publishers, Inc., New York, 1989.

[27] A. Giannopoulos, "Modelling Ground Penetrating Radar by GprMax", *Construction and Building Materials*, vol.19, pp.755-762, Aug.2005.

[28] R. Persico and F. Soldovieri, "Effects of uncertainty on background permittivity in 1D linear inverse scattering", *J. Opt. Soc. of America A.*, vol.21 (12), pp.2334-2343 Dec. 2004.

[29] F. Soldovieri, R. Persico, G. Leone, "A Microwave Tomographic Imaging Approach for Multibistatic Configuration: The Choice of the Frequency Step", *IEEE Trans. on Instr. and Meas.*, vol.55 (6), pp. 1926 – 1934, Dec. 2006.

[30] F. Soldovieri, R. Persico, G. Leone, "Effect of source and receiver radiation characteristics in subsurface prospecting within the distorted Born approximation", *Radio Sci.*, vol.40 (3), May 2005.

[31] D. Comite, A. Galli, I. Catapano, F. Soldovieri, E. Pettinelli, "An improved tomographic approach for accurate target reconstruction from GPR numerical data", *Proc. Of 15th Int. Conf. on Ground Penetrating Radar (GPR)*, pp. 611-614, July, 2014.